Spectral Analysis of Mach 6 Turbulent Boundary Layer over a Hollow Cylinder with FLDI and DNS

J. H. Chen[*], A. Hameed[†], and N. J. Parziale[‡]
Stevens Institute of Technology, Hoboken, NJ, 07030, USA

Dhiman Roy[§] and Lian Duan[¶]
The Ohio State University, Columbus, OH 43210, USA

In this paper, we present a comparison of experimental measurements of density fluctuations over a hollow cylinder to DNS data at similar conditions and wall-normal positions. The experimental observations are made using a closely-spaced multiple beam-pair FLDI flow diagnostic incorporating a technique to improve the signal-to-noise ratio, thus allowing for data to be captured above 1 MHz. The power spectral density (PSD) and two-point space-time correlations and coherence spectra computed from FLDI and DNS data are compared. The PSD spectra are further compared with expected power-law scalings in specific regions. With few deviations, good agreement is generally observed between the FLDI and DNS results and applicable power-law scalings.

I. Introduction

A thorough understanding of turbulent boundary layers at hypersonic Mach numbers is important to the design of high-speed vehicles. Turbulent boundary layers dramatically increase the aerodynamic drag and heating rate over the vehicle's surface. In tests of ballistic reentry vehicles, the surface heating rate was found to increase by a factor of 5 within the turbulent boundary layer [1]. For slender bodies, the heating rate was found to have increased by a factor of 3 following transition to the turbulent boundary layer [2, 3]. Furthermore, fluctuations in pressure within the turbulent boundary layer can induce vibrational loading on aerodynamic surfaces and impact the structural integrity of the high-speed vehicle [4, 5].

Direct numerical simulations (DNS) of high-speed turbulent boundary layers have also been conducted. Duan et al. [6] used DNS to study the pressure fluctuations generated within a turbulent boundary layer at different wall-normal locations over a flat plate. They found the dominant frequency of boundary-layer-induced pressure fluctuations shifts to lower frequencies as the location of interest moves away from the wall. Furthermore, they showed good agreement between DNS and experimental data and the expected power-law scaling in regions of low, mid, and mid-to-high overlap, and acceptable agreement at high frequencies.

Experimental investigations of hypersonic turbulent boundary layers using hot-wire anemometry have been limited by the poor frequency response and spatial resolution of the diagnostic technique [7]. Particle image velocimetry has been successfully used to measure the spatially varying velocity fields of high-speed turbulent boundary layers, however, its accuracy has been limited by the technique's particle response [7]. Pressure fluctuations within high-speed turbulent boundary layers have been limited to those at the surface and exhibit significant scatter in the magnitude of wall-pressure fluctuations [8, 9]. These measurements suffer from the poor spatial resolution of the pressure transducers or limitations in their frequency response [10].

In this paper, we study the turbulent boundary layer generated over a hollow cylinder using a non-intrusive, optical measurement technique. Developed by Smeets [11–16] and Smeets and George [17] in the 1970s, focused laser differential interferometry (FLDI) is a common path, polarizing interferometer sensitive to the phase difference between the interfering beam pairs. It features excellent spatial and temporal resolution (<100 μm and 10 MHz), as well as high sensitivity at low densities (0.1 g/m^3) [18]. In 2012, Parziale et al. [19–25] advanced the FLDI technique and used it to characterize the facility disturbance level and boundary-layer instability and transition in the Caltech T5 reflected-shock

---

*Graduate Student, Mechanical Engineering, 1 Castle Point on Hudson, Hoboken, New Jersey, 07030, USA.
†Postgraduate Scholar, Mechanical Engineering, 1 Castle Point on Hudson, Hoboken, New Jersey, 07030, USA.
‡Associate Professor, Mechanical Engineering, 1 Castle Point on Hudson, Hoboken, New Jersey, 07030, AIAA Associate Fellow.
§Graduate Research Associate, Departments of Mechanical & Aerospace Engineering, Student Member AIAA
¶Associate Professor, Department of Mechanical & Aerospace Engineering, Associate Fellow, AIAA

tunnel. Researchers have recently used the technique to make reliable measurements of convective velocity between two closely spaced FLDI probe volumes [18, 26–32], facility disturbance-level characterization [33–35], and have developed beam shaping techniques for application of the technique in hard-to-access flows [36–40]. Researchers have used controlled problems [41–43] to test the data-reduction strategies developed by Fulghum [44], Settles and Fulghum [45], Schmidt and Shepherd [46], and Hameed and Parziale [47].

The measurements of the density fluctuations obtained by the FLDI technique are compared to the DNS results. A strategy for obtaining ultra-high frequency measurements is implemented to resolve frequencies above 1 MHz. A comparison of the DNS and FLDI spectra to the expected power-law scalings in their respective regions is made. Additionally, a comparison of the correlation and coherence computed using FLDI and DNS data between two points located at various streamwise separation distances is presented.

II. Facility and Experimental Setup

All experiments performed in this work were performed at the Stevens Shock Tunnel (SST) at Stevens Institute of Technology. The SST is a reflected-shock tunnel capable of replicating Mach 6 free-flight flow conditions at an enthalpy of 1.5 MJ/kg. The facility can produce unit Reynolds numbers of 0.35 - 8.1×10^6 m^{-1} for at least 4 ms [48]. A schematic of the facility is provided in Fig. 1.
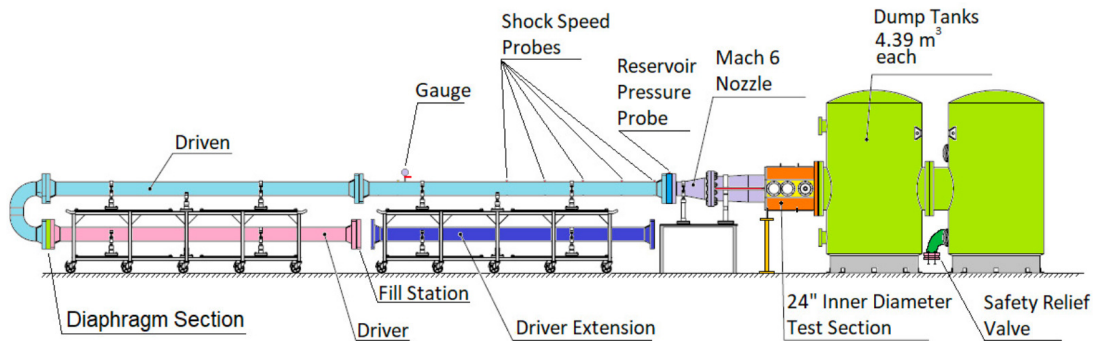

Fig. 1 Schematic of the Stevens Shock Tunnel identifying the driver and driven sections, Mach 6 nozzle, 24 inch test section, and dump tanks.

The facility is operated in a fashion similar to other shock tunnels. The driver and driven sections of the facility are separated by a double-diaphragm station, and a pair of aluminum diaphragms approximately 1.27 mm or 2.29 mm are typically used. The use of a double-diaphragm section provides a more accurate, controlled, and repeatable test method, allowing the driver pressure to be prescribed depending on the diaphragm thickness. The driven section is separated from the nozzle, test section, and dump tanks by a thinner aluminum diaphragm (typically 0.127 mm or 0.254 mm). Following the installation of the diaphragms, the entire facility is evacuated to an acceptable level of vacuum, with the test section reaching 0.25 torr. Next, the driven section is filled with the test gas (either lab air or a mixture of 5% Kr and N$_2$ to simultaneously accommodate a tagging velocimetry diagnostic technique that was employed during these experiments) to the tailored run condition, and the driver section and the double-diaphragm station are filled with N$_2$. The pressure in the double-diaphragm station is maintained at approximately half the driver pressure until the gas in the section is rapidly evacuated, beginning the experiment. The reservoir conditions were determined using the pressure of the driven tube, P$_1$, the measured incident shock speed, U$_s$ using Cantera [49] with the Shock and Detonation Toolbox [50]. The model used in these experiments was a 1 m-long hollow-cylinder flare. The model featured a sharp leading edge, a 0.102 m outer diameter hollow cylinder, and a 34° flare of maximum diameter 0.203 m. Relevant conditions for the shot analyzed in this paper (shot 385) are presented in Table 1. Here, boundary-layer quantities such as the boundary-layer thickness (δ), viscous length (y_τ), and friction velocity (u_τ), were determined in a manner similar to that described in Segall et al. [51].

Focused laser differential interferometry (FLDI) was used as the flow diagnostic for the experiments presented in this paper. The FLDI beams used to interrogate the boundary layer generated over the model were positioned approximately 0.7 m from the model's leading edge and approximately 6.7 mm above the surface of the hollow cylinder. As shown in Fig. 2a, the beam pairs were oriented in a single row of six columns, with each column interspaced by approximately 2.4

Table 1   Experimental conditions for FLDI shot 385 performed at the Stevens Shock Tunnel. Here, δ, U_e, T_w, T_r, T_w/T_r, T_∞, M_∞, Re_θ, y_τ, u_τ, and Re_τ are the boundary-layer thickness, boundary-layer edge velocity, wall temperature, recovery temperature, wall-to-recovery temperature ratio, freestream temperature, freestream Mach number, momentum thickness Reynolds number, viscous length, friction velocity, and the friction Reynolds number, respectively.

Shot	δ	U_e	T_w	T_r	T_w/T_r	T_∞	M_∞	Re_θ	y_τ	u_τ	Re_τ
	(mm)	(m/s)	(K)	(K)	(-)	(K)	(-)	(-)	(m)	(m/s)	(-)
385	13	942	295	533	0.54	65.3	6.32	8620	2.8e-05	48	450

mm. We present a magnified view of a single FLDI beam pair from this row in Fig. 2b to show the intraspacing between the pair of FLDI beams, which was determined to be approximately 0.04 mm.

The components used to generate the closely-spaced multiple beam-pair FLDI setup used as the diagnostic in these experiments are depicted in Fig. 2c. In this setup, the diffractive optical element was used to generate a single row of 6 beam pairs. The diffractive optic was also used to generate the streamwise beam interspacing seen in Fig. 2a. A Wollaston prism of 1 arcminute was used to generate the streamwise beam intraspacing. Downbeam of the test section, a complementary 1 arcminute Wollaston prism is used to recombine the intraspaced beams. Each of the twelve recombined beam pairs was focused on individual photodetectors, which register a voltage change as a result of the interference caused by the different optical path lengths traversed by the individual beams within the beam pair. The close interspacing within each row of beams required the use of an array of converging and diverging lenses (not pictured) to expand and separate the recombined beam pairs by a practical distance. Additional converging lenses were used to focus the beam onto the photodiode.
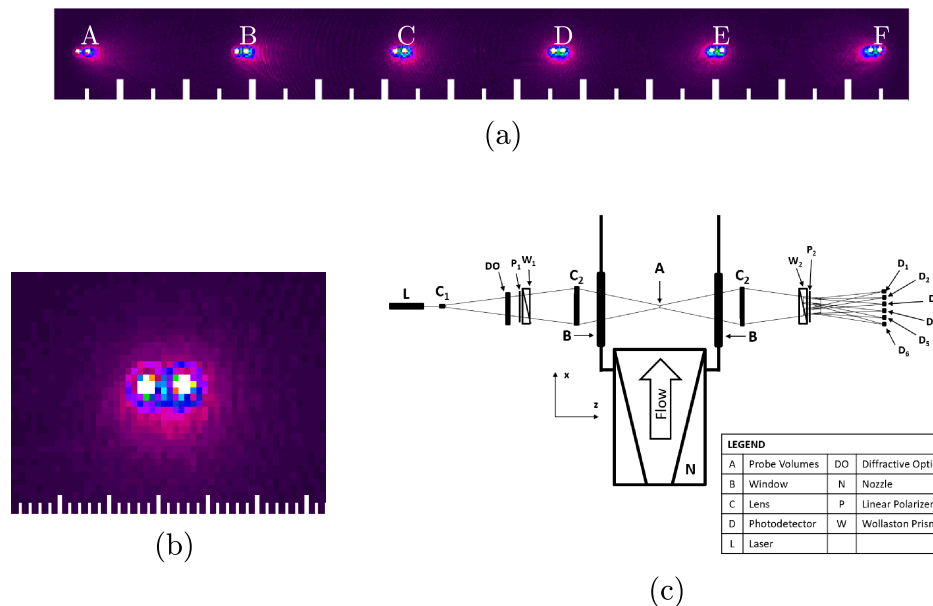

(a)

(b)

(c)

Fig. 2   (a) Picture of FLDI beam pairs taken at their focus using a beam profiling camera. The label associated with each beam pair is provided as an identifying reference. The row of FLDI beam pairs is positioned approximately 6.7 mm above the surface of the hollow-cylinder flare. Major tick marks are 1 mm apart and minor tick marks are 0.5 mm apart. (b) Close-up of an individual, closely-spaced FLDI beam pair. Here, the major and minor tick marks are 0.50 mm and 0.10 mm apart, respectively. (c) Schematic showing components used to generate the closely-spaced multiple beam-pair FLDI setup.

3

To facilitate these ultra high-frequency measurements, it was necessary to raise the FLDI signal above the noise floor. As a result, the FLDI response measured by one of the six photodetectors was passed through a high-pass filter to remove frequency content lower than 30 kHz. Next, as shown in Fig. 3, the signal was passed through a Stanford Research Systems model SR445A signal amplifier, where it was amplified by a factor of 625 before it was passed to the Cleverscope CS328A digital oscilloscope. The signals were then digitally AC-coupled in the oscilloscope to remove the DC offset. The vertical scaling of the AC-coupled Cleverscope signals was limited to slightly above/below the minimum and maximum values expected during the experiment.
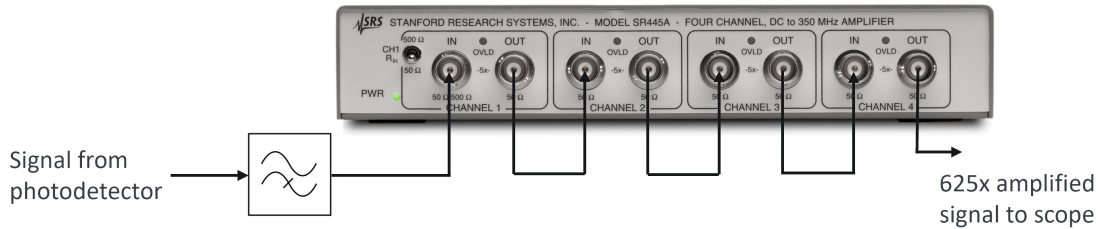

Fig. 3   Technique employed to amplify the ultra-high frequency FLDI signal above the noise floor. The amplification allowed the FLDI diagnostic to resolve frequencies above 1 MHz.

III. DNS Solutions

As mentioned in the Introduction Section, the spectra computed from FLDI data are compared with those from DNS data to understand the power-law scalings of density fluctuations. Table 2 outlines the freestream flow condition of the DNS for comparison with FLDI. The freestream condition of the DNS is similar to the conditions of the Boeing/AFOSR Mach-6 Quiet Tunnel (BAM6QT) under noisy runs with a total pressure of 921 kPa and a total temperature of 433 K. The flow conditions and setup of the present DNS are the same as those described by Duan et al. [6], except that the streamwise domain has been extended from $58.7\delta_i$ to $135.9\delta_i$ (with two overlapping computational boxes as shown in Fig. 4) to increase the range of Reynolds numbers up to $Re_\tau \simeq 660$. Additionally, the uniform region of the wall-normal grid has been extended from $5.5\delta_i$ (or 3.2δ) to $9.5\delta_i$ (or 5.5δ) to resolve a larger region of the near field of acoustic fluctuations radiated by the boundary layer (Fig. 5). Here, δ_i and δ represent boundary-layer thickness at the inflow of Box 1 and at the selected downstream location for spectral analysis, respectively. Table 3 summarizes the grid resolution and domain size for the present DNS.

The DNS solver solves the full compressible 3D Navier-Stokes equations in conservation form. The working fluid is assumed to be a perfect gas, for which the coefficient of viscosity μ is determined using Sutherland's law and the coefficient of thermal conductivity κ is calculated using $\kappa = \mu C_p / Pr$ with $Pr = 0.71$. The inviscid fluxes are discretized using a seventh-order Weighted Essentially Non-Oscillatory (WENO) scheme, which is optimized by employing limiters. A fourth-order central difference technique is used to discretize the viscous fluxes while a third-order low-storage Runge-Kutta scheme is employed for time integration, ensuring accurate and efficient computations. The top boundary utilizes an unsteady, non-reflecting boundary condition. A periodic boundary condition is applied in the spanwise direction. At the wall, a no-slip, isothermal wall condition is imposed. Additional details of the DNS methodology are provided in Duan et al. [6].

Table 2   List of freestream conditions and wall temperature, T_w for Mach 5.86 DNS of turbulent boundary layer.

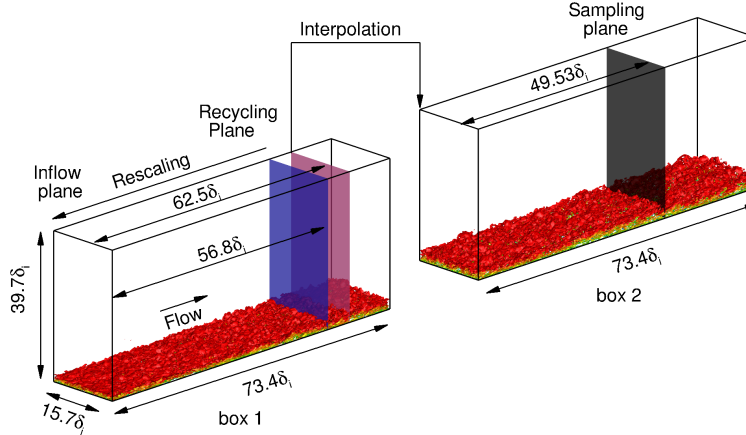| M_∞	$Re_\infty(m^{-1})$	$U_\infty(m/s)$	$\rho_\infty(kg/m^3)$	$T_\infty(K)$	$T_w(K)$
5.86	10.4×10^6	870.4	0.0427	54.97	300.0

Fig. 4   Computational domain setup for the present DNS, showing an instantaneous flow visualized by iso-surface of the magnitude of normalized density gradient, $|\Delta\rho|\delta_i/\rho_\infty = 0.98$. The iso-surface is colored by the stream-wise velocity component, which ranges from 0 to U_∞ (blue to red). $\delta_i \approx 13.8$ mm represents the boundary layer thickness at the inflow plane.

Table 3   Grid resolution and domain size for the DNS of the Mach 5.86 turbulent boundary layer. In this context, the domain sizes in the streamwise, spanwise, and wall-normal directions are normalized by the inflow boundary layer thickness, denoted by L_x/δ_i, L_z/δ_i, and L_y/δ_i respectively. The uniform grid spacings in the streamwise and spanwise directions are represented by Δx^+ and Δz^+, respectively. Additionally, Δy^+_{min} and Δy^+_{max} denote the minimum and maximum grid spacings in the wall-normal direction for $0 \leq y/\delta_i \leq 9.5$. These grid spacings are reported in terms of the viscous length scale, y_τ, evaluated at the sampling location $x/\delta_i = 49.52$. T_f is the total time for data collection. The friction velocity and the boundary layer thickness are listed in Table 4.

	L_x/δ_i	L_z/δ_i	L_y/δ_i	$N_x \times N_z \times N_y$	Δx^+	Δz^+	Δy^+_{min}	Δy^+_{max}	$T_f u_\tau/\delta$
Box 1	73.4	15.7	39.7	2000×800×700	9.7	5.2	0.51	5.3	3.8
Box 2	73.4	15.7	39.7	2000×800×700	9.7	5.2	0.51	5.3	3.0

Table 4   Boundary layer properties at the sampling plane for the Mach 5.86 turbulent boundary layer.

x_a/δ_i	Re_θ	Re_τ	$Re_{\delta2}$	θ (mm)	H	δ (mm)	y_τ (μm)	u_τ (m/s)
49.52	9530	453	1856	0.92	14.34	23.49	51.80	45.57

IV. Results

In this section, we present comparisons between the experimental results obtained at the Stevens Shock Tunnel and the DNS simulations. Specifically, the power spectral density, two-point correlation in the streamwise direction, and coherence between two points with varying spatial streamwise separation are compared.

A. Spectra Comparison

Figure 6 compares the power spectral density computed from the phase change measured by the FLDI instrument for shot 385 (black line) with the DNS spectrum of density fluctuations (red line), both at a relative wall-normal position of $y/\delta \approx 0.6$ and $Re_\tau \approx 450$. The abscissa is presented in angular frequency ($\omega = 2\pi f$). The outer-scaling normalization of the angular frequency, shown in Fig. 6a, is achieved using the respective experimental and DNS boundary-layer thickness and freestream velocity ($\omega_{norm} = \omega\delta/U_\infty$). As shown in Fig. 6b, the inner-scaling normalization of the angular frequency is performed using the viscous length and friction velocity ($\omega_{norm} = \omega y_\tau/u_\tau$) for the FLDI data
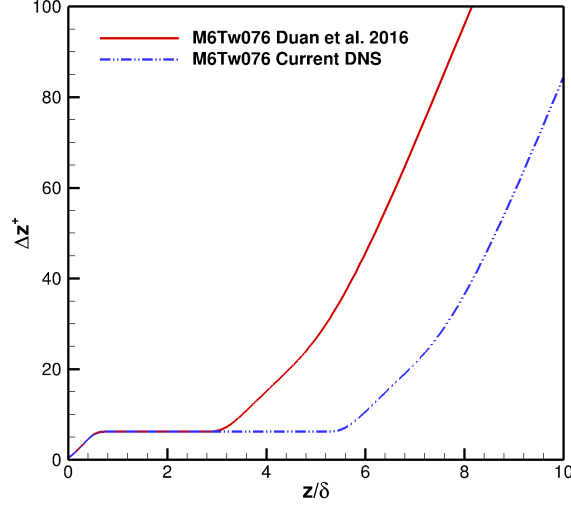
5

Fig. 5 **Comparison of wall-normal grid distribution for DNS of Mach 5.86 from Duan et al. [6] and present DNS.**

and, equivalently, the kinematic viscosity and friction velocity ($\omega_{norm} = \omega \nu_w / u_\tau^2$) for the DNS data. The expected power-law scaling in the specific regions of the spectra is provided as a reference.
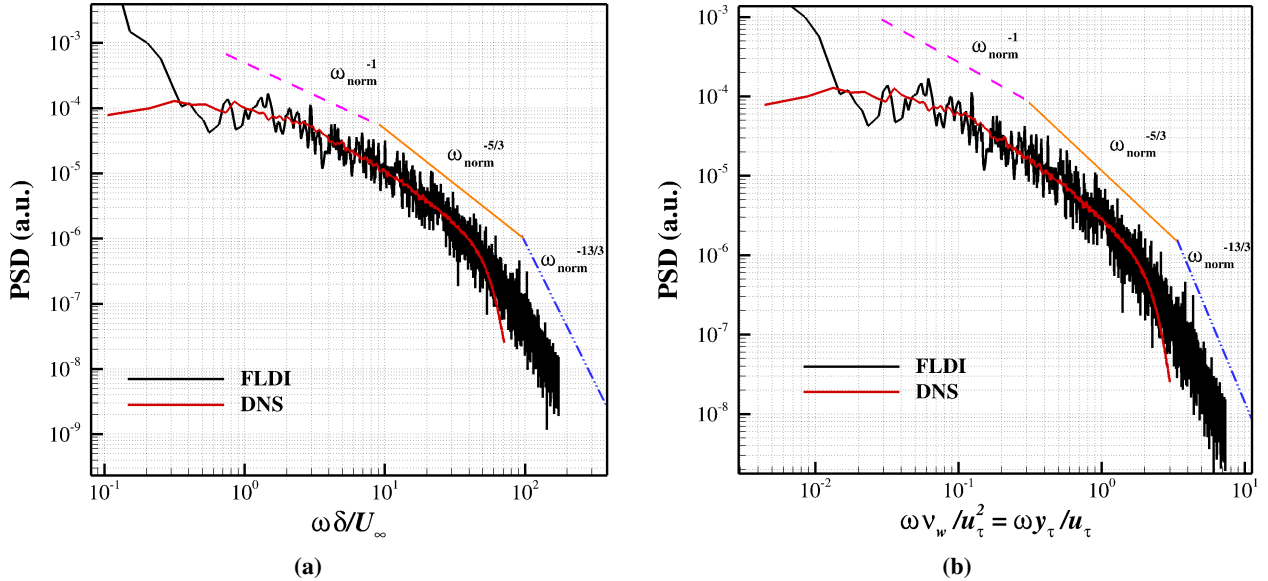

Fig. 6 **Spectra for FLDI and DNS at $y/\delta \approx 0.6$ and $Re_\tau \approx 450$. The expected power-law scalings in specific ranges of the spectra are provided as a reference. a) For outer scaling, the abscissa of both DNS and FLDI results are normalized by the respective boundary-layer thickness and freestream velocity. b) For inner scaling, the FLDI results are normalized by the viscous length and friction velocity ($\omega_{norm} = \omega y_\tau / u_\tau$) while DNS data is equivalently normalized by kinematic viscosity and friction velocity ($\omega_{norm} = \omega \nu_w / u_\tau^2$).**

Referring to 6b, the DNS spectrum briefly adheres to the ω_{norm}^{-1} scaling ($0.1 \leq \omega_{norm} \leq 0.2$) while the FLDI spectrum follows this scaling over a broader range, until $\omega_{norm} \approx 0.3$, consistent with the theoretical prediction of the estimated location of slope change from the mid to mid-to-high frequency overlap region [5]. In the mid-to-high frequency overlap region, the FLDI spectrum appears to follow the $\omega_{norm}^{-5/3}$ scaling until approximately $\omega_{norm} = 1.5$, slightly higher than the theoretically predicted transition to the high-frequency region [5]. Similarly, we observe the inertial subrange in the DNS spectrum from $0.2 \leq \omega_{norm} \leq 1.5$. In the apparent transition from the mid-to-high frequency overlap region to the high-frequency region, we observe a much more distinct divergence between the FLDI

6

and DNS spectra. At these higher normalized angular frequencies, the DNS spectrum shows a much steeper roll-off. Neither spectra appear to show extended agreement to the referenced power-law scaling in this region ($\omega_{norm}^{-13/3}$). While this scaling is provided as a reference, the spectra appear to experience a continuously changing slope at these high frequencies, making it difficult for the authors to identify a specific power-law scaling in this region. A more suitable comparison would be to compare the FLDI and DNS spectra with the model energy spectrum as defined in Pope [52], which suggests the spectra should experience exponential decay in this region. Additional analysis is needed to understand the stark deviation of the FLDI spectra from the DNS spectra at these frequencies. This difference could be a result of a misunderstanding of the spatial resolution of the FLDI instrument - further investigation is required.

B. Correlation Comparison

We next compare the correlation of density fluctuations ($C_{\rho\rho}$) calculated from DNS data to the correlations computed from experimental FLDI data. The correlation, computed using MATLAB's xcorr function, between beam pair A and subsequent beam pairs in the FLDI system (as labeled in Fig. 2) is presented in Fig. 7a. Here, the abscissa is the maximum lag time between signals, nondimensionalized by the freestream velocity and boundary-layer thickness. Expectedly, the self-correlation between FLDI signals A-A shows perfect correlation with zero time lag. As the distance from beam pair A to the subsequent beam pair increases, we observe an increase in the nondimensional time lag and an exponential decrease in the correlation coefficient. Additionally, as the nondimensional time lag increases, we observe a broadening of the correlation peak. A small deviation from the expected trend is observed in the computed correlation between signals A-C. We suspect the lower correlation coefficient computed between these signals could be due to additional noise that was present in signal C.

In Fig. 7b, we extract the peaks of the correlation coefficients computed from FLDI data in Fig. 7a and compare them to the space-time correlation of density fluctuations calculated using DNS data. For both datasets, the comparison is made at approximately the same relative height within the boundary layer ($y/\delta \approx 0.6$). The correlation is plotted as a function of the streamwise separation between probes (the interspacing between beam pairs A to F for FLDI, the distance between points for DNS) nondimensionalized by the respective boundary-layer thickness. While the FLDI correlation peaks are plotted as discrete points (due to the specific spacing between the beams and the finite number of beam pairs), a clear trend is visible, which is in excellent agreement with the decay observed in the computed correlation from DNS data. As suggested by Duan et al. [6], the correlation is sensitive to the wall-normal position, and the slightly higher values of the peak correlation coefficient computed using FLDI data could be due to uncertainty in determining the wall-normal position of the row of FLDI beams.
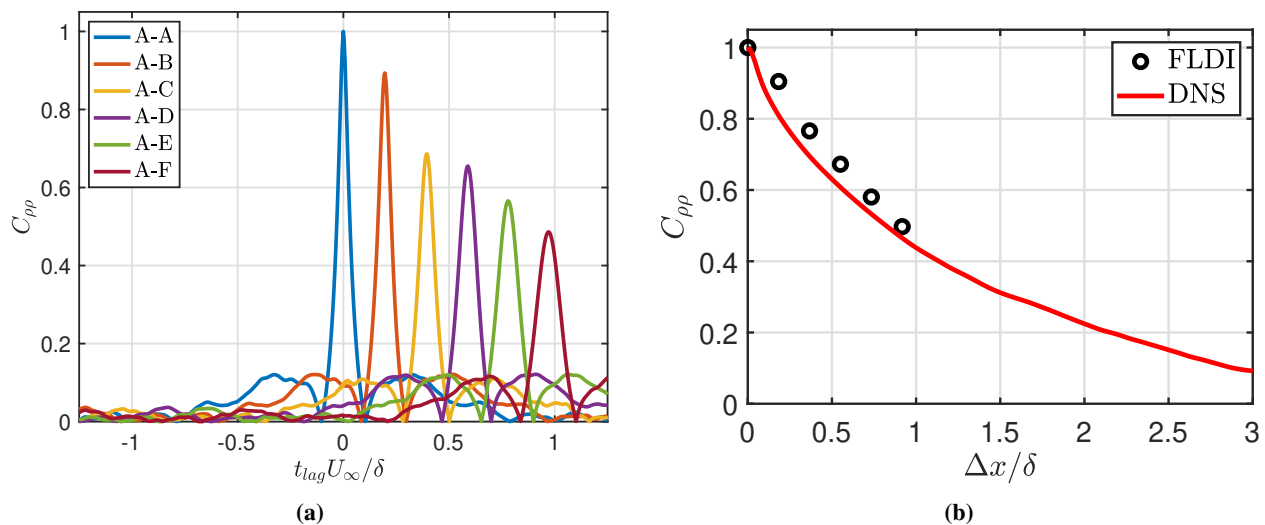

(a)

(b)

Fig. 7   a) Time domain density correlation between FLDI probes. The density correlation decreases monotonically as nondimensional time lag is increased. b) Comparison of the correlation experimentally obtained using FLDI data and computed from DNS data. The spacing between the probes (distance between beams for FLDI, points for DNS) is normalized by the respective boundary-layer thickness, δ.

C. Coherence Comparison

In this section, we compare the two-point coherence spectra computed from the FLDI and DNS data. Each DNS coherence spectra in the series presented in Fig. 8 was computed at the specific $\Delta x/\delta$ value matching the relative spacing of the FLDI beams. The FLDI and DNS spectra are plotted as functions of the angular frequency normalized by the respective boundary-layer thickness and freestream velocity. In general, we observe good agreement between the FLDI and DNS coherence spectra, noting increasing consensus between the experimental and computational datasets with decreasing streamwise spacing. As expected, the best agreement between the two coherence spectra is achieved at the smallest relative spacing, $\Delta x/\delta = 0.20$. Deviations observed in the power spectral density spectra presented in Fig. 6a also manifest in the coherence spectra. For example, the DNS coherence spectra appear to show higher values of coherence than the FLDI coherence spectra until the high-frequency region, where divergence is observed between the PSDs of the two datasets. For each relative streamwise separation, we note a significant drop in the FLDI coherence at the lower normalized angular frequencies ($\omega\delta/U_\infty \approx 0.5$), likely due to the high-pass filter used in the diagnostics's data acquisition system.
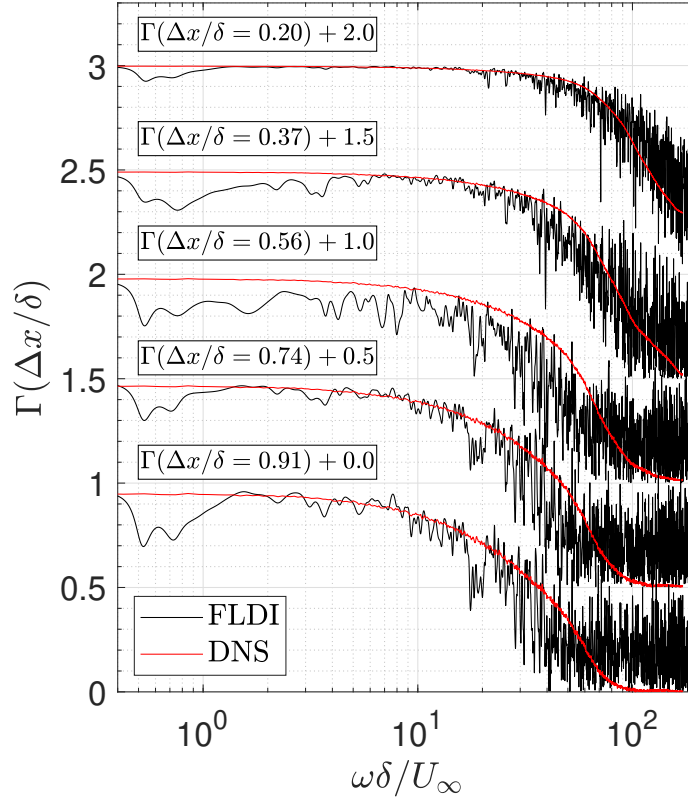

Fig. 8   Comparison of the calculated coherence between streamwise points obtained from FLDI and DNS data. The streamwise separation between points was selected to match the streamwise spacing between the FLDI beams. The DNS and FLDI frequencies are normalized by their respective boundary layer thickness and freestream velocity.

V. Conclusions

In this paper, we compare experimental measurements of density fluctuations over a hollow cylinder to DNS data at similar conditions and wall-normal positions. The experimental observations are made using a closely-spaced multiple beam-pair FLDI diagnostic. The signal-to-noise ratio of the FLDI diagnostics's output is improved using a high-pass filter, signal amplifier, and by digitally AC-coupling the signal. These modifications allowed the FLDI diagnostic to capture data above 1 MHz. A flowfield with conditions similar to those in the experiment was analyzed using DNS. The power spectral density and two-point space-time correlation and coherence computed from FLDI and DNS data were compared.

With minor deviations, the FLDI and DNS PSDs show generally good agreement. To differing extents, adherence to expected power-law scalings is observed in both spectra. The ω_{norm}^{-1} scaling is briefly observed in the uncorrected DNS spectra, while the FLDI spectra begins to follow this scaling at earlier normalized angular frequencies and to a broader extent. The $\omega_{norm}^{-5/3}$ scaling is observed in both the FLDI and DNS spectra in the mid-to-high frequency overlap region. The spectra don't appear to extensively follow the expected power-law scaling at the higher normalized angular frequencies and the FLDI spectrum deviates from the DNS spectra considerably in this region. Additional analysis is required to understand this discrepancy. We also observe a continuously changing slope in both spectra in this region. A comparison of density fluctuations computed from DNS and experimental FLDI data also shows good agreement. Although the trend is consistent with the correlation computed from DNS data, the computed experimental peak correlation coefficient is found to be higher, likely due to uncertainty in the measured wall-normal height of the row of FLDI beams and the high sensitivity of the correlation to wall-normal position. The coherence spectra shows improving agreement between the DNS and FLDI results as the streamwise spacing between the probes is decreased.

References

[1] Schneider, S. P., "Flight data for boundary-layer transition at hypersonic and supersonic speed," *Journal of Spacecraft and Rockets*, Vol. 36, No. 1, 1999, pp. 8–20. https://doi.org/10.2514/2.3428.

[2] MacLean, M., Wadhams, T., Holden, M., and Johnson, H., "Ground test studies of the HIFiRE-1 transition experiment Part 2: computational analysis," *Journal of Spacecraft and Rockets*, Vol. 45, No. 6, 2008, pp. 1149–1164. https://doi.org/10.2514/1.37693.

[3] Jewell, J. S., Parziale, N. J., Leyva, I. A., Shepherd, J. E., and Hornung, H. G., "Turbulent Spot Observations within a Hypervelocity Boundary Layer on a 5-degree Half-Angle Cone," *Proceedings of 42nd AIAA Fluid Dynamics Conference and Exhibit*, AIAA-2012-3062, New Orleans, Louisiana, 2012. https://doi.org/10.2514/6.2012-3062.

[4] Willmarth, W. W., and Yang, C. S., "Wall-pressure fluctuations beneath turbulent boundary layers on a flat plate and a cylinder," *Journal of Fluid Mechanics*, Vol. 41, 1970, pp. 47–80. https://doi.org/10.1017/S0022112070000526.

[5] Bull, M. K., "Wall-pressure fluctuations beneath turbulent boundary layers: some reflections on forty years of research," *Journal of Sound and Vibration*, Vol. 190, 1996, pp. 299–315. https://doi.org/10.1006/jsvi.1996.0066.

[6] Duan, L., Choudhari, M. M., and Zhang, C., "Pressure fluctuations induced by a hypersonic turbulent boundary layer," *Journal of Fluid Mechanics*, Vol. 804, 2016, pp. 578–607. https://doi.org/10.1017/jfm.2016.548.

[7] Williams, O. J. H., Sahoo, D., Baumgartner, M. L., and Smits, A. J., "Experiments on the structure and scaling of hypersonic turbulent boundary layers," *Journal of Fluid Mechanics*, Vol. 834, 2018, pp. 237–270. https://doi.org/10.1017/jfm.2017.712.

[8] Kistler, A. L., and Chen, W. S., "The fluctuating pressure field in a supersonic turbulent boundary layer," *Journal of Fluid Mechanics*, Vol. 16, 1963, pp. 41–64. https://doi.org/10.1017/S0022112063000574.

[9] Beresh, S. J., Henfling, J. F., Spillers, R. W., and Pruett, B. O., "Fluctuating wall pressures measured beneath a supersonic turbulent boundary layer," *Physics of Fluids*, Vol. 23, No. 7, 2011, p. 075110. https://doi.org/10.1063/1.3609271.

[10] Fernholz, H. H., Dussauge, J. P., Finlay, P. J., Smits, A. J., and Reshotko, E., "A survey of measurements and measuring techniques in rapidly distorted compressible turbulent boundary layers," Tech. rep., ADVISORY GROUP FOR AEROSPACE RESEARCH AND DEVELOPMENT NEUILLY-SUR-SEINE (FRANCE), 1989.

[11] Smeets, G., and George, A., "Gas Dynamic Investigations in a Shock Tube using a Highly Sensitive Interferometer," Translation of ISL Internal Report 14/71, Original 1971, Translation 1996.

[12] Smeets, G., "Laser Interferometer for High Sensitivity Measurements on Transient Phase Objects," *IEEE Transactions on Aerospace and Electronic Systems*, Vol. AES-8, No. 2, 1972, pp. 186–190. https://doi.org/10.1109/TAES.1972.309488.

[13] Smeets, G., and George, A., "Anwendungen des Laser-Differentialinterferometers in der Gasdynamik," ISL - N 28/73, Also translated by Goetz, A.: ADA-307459, 1973.

[14] Smeets, G., "Laser-Interferometer mit grossen, fokussierten Lichtbündeln für lokale Messungen," ISL - N 11/73, 1973.

[15] Smeets, G., "Verwendung eines Laser-Differentialinterferometers zur Bestimmung lokaler Schwankungsgrössen sowie des mittleren Dichteprofils in cinem turbulenten Freistrahl," ISL - N 20/74, 1974.

[16] Smeets, G., "Flow Diagnostics by Laser Interferometry," *IEEE Transactions on Aerospace and Electronic Systems*, Vol. AES-13, No. 2, 1977, pp. 82–90. https://doi.org/10.1109/TAES.1977.308441.

[17] Smeets, G., and George, A., "Laser Differential Interferometer Applications in Gas Dynamics," Translation of ISL Internal Report 28/73, Original 1975, Translation 1996.

[18] Ceruzzi, A. P., and Cadou, C. P., "Simultaneous Velocity and Density Gradient Measurements using Two-Point Focused Laser Differential Interferometry," *Proceedings of AIAA Scitech 2019*, AIAA-2019-2295, San Diego, California, 2019. https://doi.org/10.2514/6.2019-2295.

[19] Parziale, N. J., Shepherd, J. E., and Hornung, H. G., "Reflected Shock Tunnel Noise Measurement by Focused Differential Interferometry," *Proceedings of 42nd AIAA Fluid Dynamics Conference and Exhibit*, AIAA-2012-3261, New Orleans, Louisiana, 2012. https://doi.org/10.2514/6.2012-3261.

[20] Parziale, N. J., Jewell, J. S., Shepherd, J. E., and Hornung, H. G., "Optical Detection of Transitional Phenomena on Slender Bodies in Hypervelocity Flow," *Proceedings of RTO Specialists Meeting AVT-200/RSM-030 on Hypersonic Laminar-Turbulent Transition*, NATO, San Diego, California, 2012.

[21] Parziale, N. J., Shepherd, J. E., and Hornung, H. G., "Differential Interferometric Measurement of Instability at Two Points in a Hypervelocity Boundary Layer," *Proceedings of 51st AIAA Aerospace Sciences Meeting Including the New Horizons Forum and Aerospace Exposition*, AIAA-2013-0521, Grapevine, Texas, 2013. https://doi.org/10.2514/6.2013-521.

[22] Parziale, N. J., Shepherd, J. E., and Hornung, H. G., "Differential Interferometric Measurement of Instability in a Hypervelocity Boundary Layer," *AIAA Journal*, Vol. 51, No. 3, 2013, pp. 750–753. https://doi.org/10.2514/1.J052013.

[23] Parziale, N. J., "Slender-Body Hypervelocity Boundary-Layer Instability," Ph.D. thesis, California Institute of Technology, 2013.

[24] Parziale, N. J., Shepherd, J. E., and Hornung, H. G., "Free-stream density perturbations in a reflected-shock tunnel," *Experiments in Fluids*, Vol. 55, No. 2, 2014, p. 1665. https://doi.org/10.1007/s00348-014-1665-0.

[25] Parziale, N. J., Shepherd, J. E., and Hornung, H. G., "Observations of hypervelocity boundary-layer instability," *Journal of Fluid Mechanics*, Vol. 781, 2015, pp. 87–112. https://doi.org/10.1017/jfm.2015.489.

[26] Jewell, J. S., Parziale, N. J., Lam, K.-L., Hagen, B. J., and Kimmel, R. L., "Disturbance and Phase Speed Measurements for Shock Tubes and Hypersonic Boundary-Layer Instability," *Proceedings of 32nd AIAA Aerodynamic Measurement Technology and Ground Testing Conference*, AIAA-2016-3112, Washington, D. C., 2016. https://doi.org/10.2514/6.2016-3112.

[27] Jewell, J. S., Hameed, A., Parziale, N. J., and Gogineni, S. P., "Disturbance Speed Measurements in a Circular Jet via Double Focused Laser Differential Interferometry," *Proceedings of AIAA Scitech 2019*, AIAA-2019-2293, San Diego, California, 2019. https://doi.org/10.2514/6.2019-2293.

[28] Ceruzzi, A. P., Callis, B., Weber, D., and Cadou, C. P., "Application of Focused Laser Differential Interferometry (FLDI) in a Supersonic Boundary Layer," *Proceedings of AIAA Scitech 2020*, AIAA-2020-1973, Orlando, Florida, 2020. https://doi.org/10.2514/6.2020-1973.

[29] Weisberger, J. M., Bathel, B. F., Herring, G. C., King, R. A., Chou, A., and Jones, S. B., "Two-Point Focused Laser Differential Interferometry Second-Mode Measurements at Mach 6," *Proceedings of AIAA Aviation Forum*, AIAA-2019-2903, Dallas, Texas, 2019. https://doi.org/10.2514/6.2019-2903.

[30] Bathel, B. F., Weisberger, J. M., Herring, G. C., King, R. A., Jones, S. B., Kennedy, R. E., and Laurence, S. J., "Two-point, parallel-beam focused laser differential interferometry with a Nomarski prism," *Applied Optics*, Vol. 59, No. 2, 2020, pp. 244–252. https://doi.org/10.1364/AO.59.000244.

[31] Price, T. J., Gragston, M., Schmisseur, J. D., and Kreth, P. A., "Measurement of supersonic jet screech with focused laser differential interferometry," *Applied Optics*, Vol. 59, No. 28, 2020, pp. 8902–8908. https://doi.org/10.1364/AO.402011.

[32] Hameed, A., Parziale, N. J., Paquin, L., Butler, C., and Laurence, S. J., "Spectral Analysis of a Hypersonic Boundary Layer on a Right, Circular Cone," *Proceedings of AIAA SciTech 2020*, AIAA-2020-0362, Orlando, Florida, 2020, pp. 1–14. https://doi.org/10.2514/6.2020-0362.

[33] Harris, A. J., Kreth, P. A., Combs, C. S., and Schmisseur, J. D., "Laser Differential Interferometry and Schlieren as an Approach to Characterizing Freestream Disturbance Levels," *2018 AIAA Aerospace Sciences Meeting*, AIAA 2018-1100, Kissimmee, Florida, 2018. https://doi.org/10.2514/6.2018-1100.

[34] Lawson, J. M., and Austin, J. M., "Expansion Tube Freestream Disturbance Measurements using a Focused Laser Differential Interferometer," *Proceedings of AIAA Scitech 2020*, AIAA-2020-1064, Orlando, Florida, 2020. https://doi.org/10.2514/6.2020-1064.

[35] Birch, B., Buttsworth, D., and Zander, F., "Measurements of freestream density fluctuations in a hypersonic wind tunnel," *Experiments in Fluids*, Vol. 61, No. 158, 2020, pp. 1–13. https://doi.org/10.1007/s00348-020-02992-w.

[36] Hedlund, B., Houpt, A., Gordeyev, S., and Leonov, S., "Measurement of Flow Perturbation Spectra in Mach 4.5 Corner Separation Zone," *AIAA Journal*, Vol. 56, No. 7, 2018, pp. 2699–2711. https://doi.org/10.2514/1.J056576.

[37] Houpt, A. W., and Leonov, S. B., "Focused Laser Differential Interferometer for Supersonic Boundary Layer Measurements on Flat Plate Geometries," *Proceedings of the 2018 Plasmadynamics and Lasers Conference*, AIAA-2018-3434, Atlanta, Georgia, 2018. https://doi.org/10.2514/6.2018-3434.

[38] Houpt, A. W., and Leonov, S. B., "Focused and Cylindrical-Focused Laser Differential Interferometer Characterization of SBR-50 at Mach 2," *Proceedings of AIAA Aviation 2019*, AIAA-2019-3383, Dallas, Texas, 2019. https://doi.org/10.2514/6.2019-3383.

[39] Benitez, E. K., Jewell, J. S., and Schneider, S. P., "Focused Laser Differential Interferometry for Hypersonic Flow Instability Measurements with Contoured Tunnel Windows," *Proceedings of AIAA Scitech 2020*, AIAA-2020-1282, Orlando, Florida, 2020. https://doi.org/10.2514/6.2020-1282.

[40] Benitez, E. K., Esquieu, S., Jewell, J. S., and Schneider, S. P., "Instability Measurements on an Axisymmetric Separation Bubble at Mach 6," *Proceedings of AIAA Aviation 2020*, AIAA-2020-3072, Virtual Event, 2020. https://doi.org/10.2514/6.2020-3072.

[41] Ramprakash, A., McIntyre, T. J., Wheatley, V., and Mee, D. J., "Performance Analysis of FLDI Technique using Turbulent Jets," *Proceedings of the IX Australian Conference on Laser Diagnostics*, Adelaide, Australia, 2019.

[42] Lawson, J. M., Neet, M. C., Grossman, I. J., and Austin, J. M., "Characterization of a Focused Laser Differential Interferometer," *Proceedings of AIAA Scitech 2019*, AIAA-2019-2296, San Diego, California, 2019. https://doi.org/10.2514/6.2019-2296.

[43] Lawson, J. M., Neet, M. C., Grossman, I. J., and Austin, J. M., "Static and dynamic characterization of a focused laser differential interferometer," *Experiments in Fluids*, Vol. 61, No. 187, 2020, pp. 1–11. https://doi.org/10.1007/s00348-020-03013-6.

[44] Fulghum, M. R., "Turbulence measurements in high-speed wind tunnels using focusing laser differential interferometry," Ph.D. thesis, The Pennsylvania State University, 2014.

[45] Settles, G. S., and Fulghum, M. R., "The Focusing Laser Differential Interferometer, an Instrument for Localized Turbulence Measurements in Refractive Flows," *Journal of Fluids Engineering*, Vol. 138, No. 10, 2016, p. 101402. https://doi.org/10.1115/1.4033960.

[46] Schmidt, B. E., and Shepherd, J. E., "Analysis of focused laser differential interferometry," *Applied Optics*, Vol. 54, No. 28, 2015, pp. 8459–8472. https://doi.org/10.1364/AO.54.008459.

[47] Hameed, A., and Parziale, N. J., "Focused Laser Differential Interferometry Transfer Functions for Complex Density Disturbance Fields," *Proceedings of AIAA Aviation Forum 2021*, AIAA-2021-2907, Virtual Event, 2021. https://doi.org/10.2514/6.2021-2907.

[48] Shekhtman, D., Hameed, A., Segall, B. A., Dworzanczyk, A. R., and Parziale, N. J., "Initial Shakedown Testing of the Stevens Shock Tunnel," *Proceedings of AIAA SciTech 2022*, AIAA 2022-1402, San Diego, California and Virtual Event, 2022. https://doi.org/10.2514/6.2022-1402.

[49] Goodwin, D. G., "An Open-Source, Extensible Software Suite for CVD Process Simulation," *Proceedings of CVD XVI and EuroCVD Fourteen, M Allendorf, F Maury, and F Teyssandier (Eds.)*, 2003, pp. 155–162.

[50] Browne, S., Ziegler, J., and Shepherd, J. E., "Numerical Solution Methods for Shock and Detonation Jump Conditions," GALCIT - FM2006-006, Caltech, 2006.

[51] Segall, B. A., Shekhtman, D., Hameed, A., Chen, J. H., and Parziale, N. J., "Profiles of streamwise velocity and fluctuations in a hypersonic turbulent boundary layer using acetone tagging velocimetry," *Experiments in Fluids*, Vol. 64, 2023, p. 122. https://doi.org/10.1007/s00348-023-03647-2.

[52] Pope, S. B., *Turbulent Flows*, 1st ed., Cambridge University Press, 2000.